resistance of multilayers depends on the magnetic coupling, a small external field can be registered.

Finally, we note that although the basic idea behind this work is that new non-collinear magnetic configurations of multi-layer systems can be stabilized, the actual numbers calculated here for appropriate thicknesses are connected to some uncertainties. We have assumed, for instance, that the contribution given by the MAE in Fig. 1 is insensitive to the influence of the spacer layer. In addition, we have neglected the magnetic dipole contribution[5] (which is indeed small for this system). The largest cause of error presented here is the calculated value of the interlayer exchange coupling, since previous work shows that the calculated strength is typically overestimated, compared to experimental measurements, by a factor of 5–10. In order to mimic an experimental situation as closely as possible we therefore reduced the calculated strength of the interlayer exchange coupling by a factor of 5. In order to analyse how different values of the interlayer exchange coupling influences the proposed multilayer we show in Fig. 2 the difference in angle, $\Delta\phi$, as a function of V thickness, for calculations with different strengths of the interlayer exchange coupling. The most conspicuous feature of the behaviour of $\Delta\phi$ as a function of spacer thickness is not modified by the strength of the exchange coupling; merely, the damping strength is influenced. Also, without the influence of the MAE the magnetization simply oscillates between ferro- and antiferromagnetic, whereas a non-negligible MAE produces a smoother behaviour in the coupling between different layers. Hence, these sources of error do not change the basic idea put forward here, that non-collinear, essentially perpendicular magnets may be grown, and that this is caused by a competition between interlayer exchange coupling and the MAE. This competition produces a magnetization profile that varies more smoothly with spacer thickness, and also reduces the energy between different magnetic configurations. We note here the difference from a conventional exchange-coupled sensor, that in theory could be tuned to a small coupling energy by getting close to a node in the oscillating exchange coupling curve. Owing to the large sensitivity to the exact thickness, such a set-up is useless in reality and has not been realized experimentally. In our proposed device, we suggest tuning the spacer-layer thickness to a local maximum in coupling strength; this is done in practice in conventional sensors.

The suggested multilayer sensor has, in certain aspects, a similar performance to conventional sensors, but with increased sensitivity, and from a technical process viewpoint we can draw on the experience of these systems. The precise number of atomic layers needed to optimize the proposed device must be determined experimentally. An extensive experimental study is needed to fine-tune the optimal choice of materials combinations and thicknesses. Other candidates of interest, in the sense that they have MAE stabilizing perpendicular magnetism in a strained state, are Ni and Co separated by an fcc spacer layer such as Cu, Pd or Pt. In addition, Pt has a large spin-orbit coupling the enhances the MAE values. □

Received 1 October 1999; accepted 17 May 2000.

1. Baibich, M. N. *et al.* Giant magnetoresistance of (001)Fe/(001)Cr magnetic superlattices. *Phys. Rev. Lett.* **61,** 2472–2475 (1988).
2. Parkin, S. S. P., More, N. & Roche, K. P. Oscillations in exchange coupling and magnetoresistance in metallic superlattice structures: Co/Ru, Co/Cr, and Fe/Cr. *Phys. Rev. Lett.* **64,** 2304–2307 (1990).
3. Binasch, G., Grünberg, P., Saurenbach, F. & Zinn, W. Enhanced magnetoresistance in layered magnetic structures with antiferromagnetic interlayer exchange. *Phys. Rev. B* **39,** 4828–4830 (1989).
4. Bruno, P. Theory of interlayer magnetic coupling. *Phys. Rev. B* **52,** 411–439 (1995).
5. Aharoni, A. *Introduction to the Theory of Ferromagnetism* (Oxford Science, Oxford, 1996).

Acknowledgements

Support from J. M. Wills is acknowledged. This project has been financed by the Swedish Natural Science and Technical Research Councils (NFR and TFR). Support for the European programme, Training and Mobility of Researchers (TMR) is acknowledged.

Correspondence and requests for materials should be addressed to B.J. (e-mail: borje.johansson@fysik.uu.se).

Imaging the vortex-lattice melting process in the presence of disorder

Alex Soibel*, Eli Zeldov*, Michael Rappaport†, Yuri Myasoedov*, Tsuyoshi Tamegai‡¶, Shuuichi Ooi ‡, Marcin Konczykowski§ & Vadim B. Geshkenbein‖

* *Department of Condensed Matter Physics, The Weizmann Institute of Science, Rehovot 76100, Israel*
† *Physics Services, The Weizmann Institute of Science, Rehovot 76100, Israel*
‡ *Department of Applied Physics, The University of Tokyo, Hongo, Bunkyo-ku, Tokyo 113-8656, Japan*
§ *CNRS, UMR 7642, Laboratoire des Solides Irradies, Ecole Polytechnique, 91128 Palaiseau, France*
‖ *Theoretische Physik, ETH-Honggerberg, CH-8093 Zurich, Switzerland, & L. D. Landau Institute for Theoretical Physics, 117940 Moscow, Russia*
¶ *CREST, Japan Science and Technology Corporation (JST), Japan*

General arguments[1] suggest that first-order phase transitions become less sharp in the presence of weak disorder, while extensive disorder can transform them into second-order transitions; but the atomic level details of this process are not clear. The vortex lattice in superconductors provides a unique system in which to study the first-order transition[2–6] on an inter-particle scale, as well as over a wide range of particle densities. Here we use a differential magneto-optical technique to obtain direct experimental visualization of the melting process in a disordered superconductor. The images reveal complex behaviour in nucleation, pattern formation, and solid–liquid interface coarsening and pinning. Although the local melting is found to be first-order, a global rounding of the transition is observed; this results from a disorder-induced broad distribution of local melting temperatures, at scales down to the mesoscopic level. We also resolve local hysteretic supercooling of microscopic liquid domains, a non-equilibrium process that occurs only at selected sites where the disorder-modified melting temperature has a local maximum. By revealing the nucleation process, we are able to experimentally evaluate the solid–liquid surface tension, which we find to be extremely small.

We first discuss the expected vortex-lattice melting process in the absence of disorder. Under equilibrium magnetization conditions in platelet-shaped samples in perpendicular applied field $H_a \| z$, the internal fields $B(x,y)$ and $H(x,y)$ across the sample have a dome-shaped profile with a maximum at the centre[7]. This is because in the absence of bulk pinning, the equilibrium shielding currents flow only along the sample edges. As H_a or temperature T is increased, the field H in the central part of the sample reaches the melting field $H_m(T)$ first, and thus a small round 'puddle' of vortex liquid should be formed in the centre, surrounded by vortex solid. Because of the first-order nature of the transition, the vortex-lattice melting is associated with a discontinuous step in the equilibrium magnetization[6], $4\pi\Delta M = \Delta(B - H)$. Because in our geometry H is continuous across the solid–liquid interface, the field B in the liquid is enhanced by ΔB relative to the solid. In $Bi_2Sr_2CaCu_2O_8$ (BSCCO) crystals ΔB is typically[6] 0.1–0.4 G. Conventional magneto-optical (MO) imaging techniques[8–10] (Fig. 1 legend) cannot resolve such small field differences. We have therefore devised the following differential method.

An MO image is acquired by averaging typically ten charge-coupled device (CCD) images at some H_a and T. Then H_a is increased by $\delta H_a \ll H_a$, or T is increased by $\delta T \ll T$, a second averaged image is obtained, and subtracted from the first. This process is averaged typically 100 times, yielding a differential field resolution of about 30 mG, approximately two orders of magnitude better than the standard MO method. By recording the differential

images in a sequence of fields or temperatures a 'movie' of the melting process is obtained.

As H_a is increased by δH_a, the radius of the vortex-liquid puddle should ideally increase by δR, determined by the gradient of the dome-shaped profile $H(x,y)$. The differential image in this case should show a bright ring on a dark background, which indicates the location of the expanding solid–liquid interface. In the rest of the image almost no change in the field should occur, except the uniform background signal of δH_a. The intensity of the ring is ΔB above the background[11], independent of δH_a, whereas the width of the ring reflects the distance δR over which the interface expands due to δH_a. This is the expected equilibrium coexistence of the solid and liquid phases due to an intrinsic gradient of the internal field, similar to the phase separation of water and ice in the presence of a gravitational field. However, we find that the phase separation is governed by the disorder, and the dome-shaped field profile merely delays the melting process near the edges.

Figure 1a presents differential MO images from the vortex-lattice melting 'movie' in one of the smaller BSCCO crystals, which is initially in the vortex solid phase. At 159.5 Oe a small liquid puddle is nucleated, seen as a bright spot in the upper-right corner. In contrast to expectations, the puddle is not in the centre of the sample, nor is it round; instead, a rather rough shape of the liquid domain is observed. As H_a is further increased a ring-like bright object is obtained, which is the solid–liquid interface separating the liquid from the surrounding vortex solid. Both the shape and the width of the ring are highly non-uniform. At 165 Oe a 'tongue' of the liquid protrudes sharply to the left side. Figure 1b shows the corresponding outer contours of the liquid phase at 0.5 Oe intervals of H_a. The interface is often pinned, resulting in overlapping contours, and then bursts out to more remote locations by a sequence of irregular local protrusions with a high degree of corrugation.

We now show that the observed complexity of the melting process is the result of disorder. Theoretical arguments[1] suggest that disorder in solids causes local variations in the melting field H_m, resulting in a rough $T_m(x,y)$ or $H_m(x,y)$ 'landscape', and the distribution function of the local melting field $f_m(H)$ develops characteristic tails on both sides of the mean field H_m^0. In high-temperature superconductors, point disorder as well as anisotropy are known to shift[12] H_m^0, and therefore local variations in these parameters[13], quenched during crystal growth, should be the main source of the roughening of the $H_m(x,y)$ landscape and the broadening of $f_m(H)$, as illustrated in Fig. 2a.

In order to analyse this process quantitatively, Fig. 2b shows a partial set of melting images in a large BSCCO crystal with three visible crystallographic defects. The vortex-liquid phase of a very irregular shape is formed initially at 91.5 Oe in the lower left corner (blue). At 92.5 Oe a separate liquid region appears along one of the defects. With increasing H_a very complex patterns of intermixed solid and liquid regions are formed. The dominant effect of the crystallographic disorder is clearly visible here because the melting

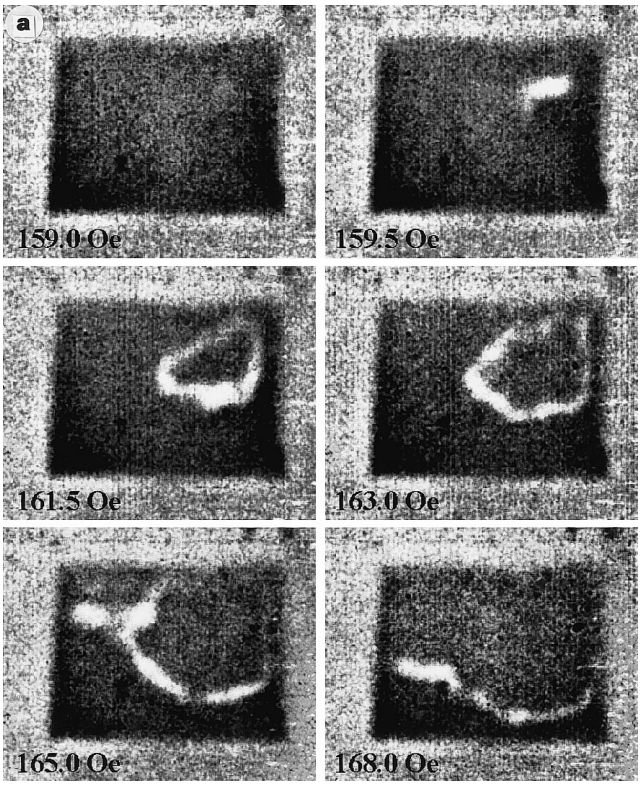

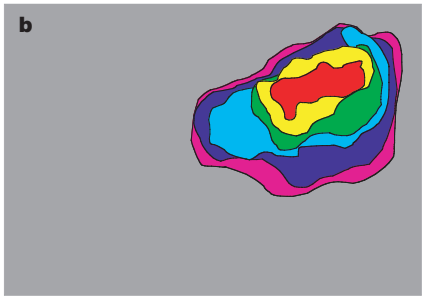

Figure 1 Vortex-lattice melting process in a small BSCCO crystal. Magneto-optical (MO) imaging[8–10] is achieved by placing a garnet indicator film on a sample. Linearly polarized light undergoes Faraday rotation in the indicator and is reflected back through a crossed polarizer, resulting in a real-time image of the magnetic field distribution. **a**, Differential MO images of the melting process in a BSCCO crystal (T_c = 60 K) of area 0.35 × 0.27 mm^2 at T = 60 K and $H_a \| c$-axis. (The full movie is available at http://www.weizmann.ac.il/home/fnsup). The grayscale from black to white spans a field range of 0.2 G. The region outside the sample is bright. The differential images are obtained by subtracting the image at field H_a from the image at $H_a + \delta H_a$, with δH_a = 1 Oe. At 159.5 Oe a small liquid droplet is nucleated within a solid resulting in the bright spot. Increasing H_a to 161.5 and 163.0 Oe, the liquid phase expands, seen as a dark region surrounded by a bright ring. The local width of the ring reflects the extent of the propagation of the solid–liquid interface due to the field modulation δH_a. The entire upper part is in the liquid phase at 168.0 Oe. **b**, Contours of the liquid phase at H_a = 159.5, 160.0, 160.5, 161.0, 161.5 and 162.0 Oe. The propagation of the solid–liquid interface is characterized by pinning and local protrusions resulting in a rough structure. The contours can be viewed as equipotential lines of $H_m(x,y)$ landscape (see Fig. 2a). Overlapping contours indicate an interface which is pinned due to steep variations in $H_m(x,y)$. As H_a is increased from 159.5 Oe (red) to 160.0 Oe (yellow) the interface remains pinned at the right and left edges, but expands upwards and downwards. The upper part remains pinned at 160.5 Oe (green) and 161.0 Oe (cyan), then expands abruptly at 161.5 Oe and gets pinned again at 162.0 Oe.

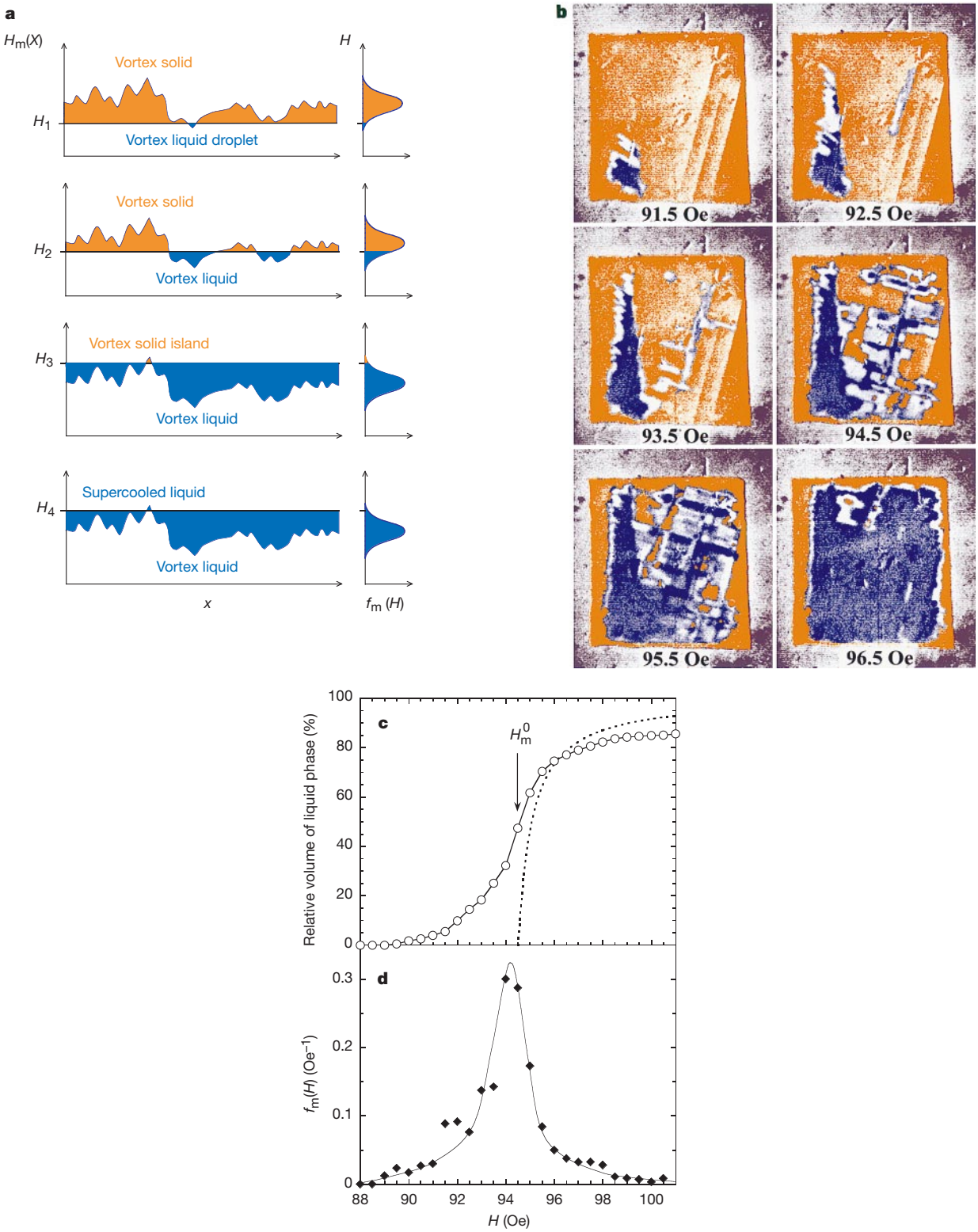

Figure 2 Melting process in the presence of disorder. **a**, Schematic plot of $H_m(x)$ landscape and the distribution function $f_m(H)$, for various values of the field H. When $H = H_1$ in the low-field tail of $f_m(H)$, a small liquid droplet (blue) is nucleated at the minimum of $H_m(x)$. As H is increased to H_2, large liquid domains are formed. A small solid island is present within the liquid at H_3, in the high-field tail of $f_m(H)$. After complete melting and upon reduction of the field to $H_4 = H_3$, the solid island is found to be absent, giving rise to a supercooled liquid domain and hysteretic local behaviour. **b**, Melting process in a large BSCCO crystal of $1.1 \times 1.2 \times 0.025\ mm^3$ at $T = 70$ K and $\delta H_a = 1$ Oe, demonstrating the effects of disorder. (The full movie is available at http://www.weizmann.ac.il/home/fnsup). The solid and liquid regions are shown in brown and blue, respectively. At 91.5 Oe an irregular liquid droplet is formed in the lower left corner. On the right-hand side three parallel crystallographic defects are visible. The crystallographic disorder in the sample has characteristic directions aligned parallel and perpendicular to the crystal growth direction, inducing corresponding features in the $H_m(x,y)$ landscape. As a result, complicated melting patterns are resolved at 93.5, 94.5 and 95.5 Oe with numerous solid and liquid domains. At 96.5 Oe a large liquid region is present in the centre, with a few solid islands in the top part. **c**, Liquid volume fraction versus H_a obtained from the full melting sequence, showing the global rounding of the melting transition with characteristic tails above and below the mean field H_m^0. The dashed line shows the calculated liquid fraction in the absence of disorder, due to the dome-shaped internal field profile. **d**, The experimental distribution function of the melting field $f_m(H)$ obtained by taking the derivative of the vortex liquid volume in **c** with respect to the field H. The solid line is a guide to the eye.

patterns have well defined preferential directions aligned parallel and perpendicular to the defects. Figure 2c presents the volume fraction of the liquid versus H_a, which allows a derivation of the distribution function $f_m(H)$ shown in Fig. 2d. Although locally the melting is a sharp first-order transition, the global solid–liquid transformation is completely rounded, and $f_m(H)$ displays pronounced tails extending both below and above H_m^0. This general form of $f_m(H)$, which we observe in all the samples, is in agreement with the theoretical predictions[1]. The dashed line in Fig. 2c shows for comparison the calculated melting behaviour in the absence of disorder, resulting from the fit to the experimental dome-shaped field profile across the sample. In this case the melting should set in abruptly, and most of the volume should melt within a few Oe from H_m^0. Thus the disorder is dominant in the observed rounding of the transition and in the development of $f_m(H)$ tails.

We present several examples of the melting features in various crystals. Figure 3a shows an enlarged view of nucleation of two liquid droplets in the low-field tail of $f_m(H)$. The width of the smaller droplet is below 6 μm (close to our resolution limit), which means that this droplet is less than seven vortices wide. This image is a striking demonstration that the disorder-nucleated melting occurs on a mesoscopic level. Furthermore, it shows that the solid–liquid surface tension is very low, as addressed below. Such liquid droplets, formed at local minima of $H_m(x,y)$ (see Fig. 2a), are found to behave reversibly with field, in contrast to solid islands at maxima of $H_m(x,y)$, as described below. Another example of liquid nucleation in a different BSCCO crystal is shown in Fig. 3b. Here the nucleation occurs simultaneously in three adjacent regions, demonstrating specific correlations in the disorder distribution quenched during crystal growth. The characteristic width of the solid and liquid patterns is about 25 μm (34 vortices), further indicating low surface tension. High surface tension would prevent such proximity of microscopic domains, favouring formation of a single larger liquid region. With increasing H_a large liquid domains of irregular shape are formed, as demonstrated in Fig. 3c. Here a highly irregular ring separates the vortex liquid from the surrounding solid. The local

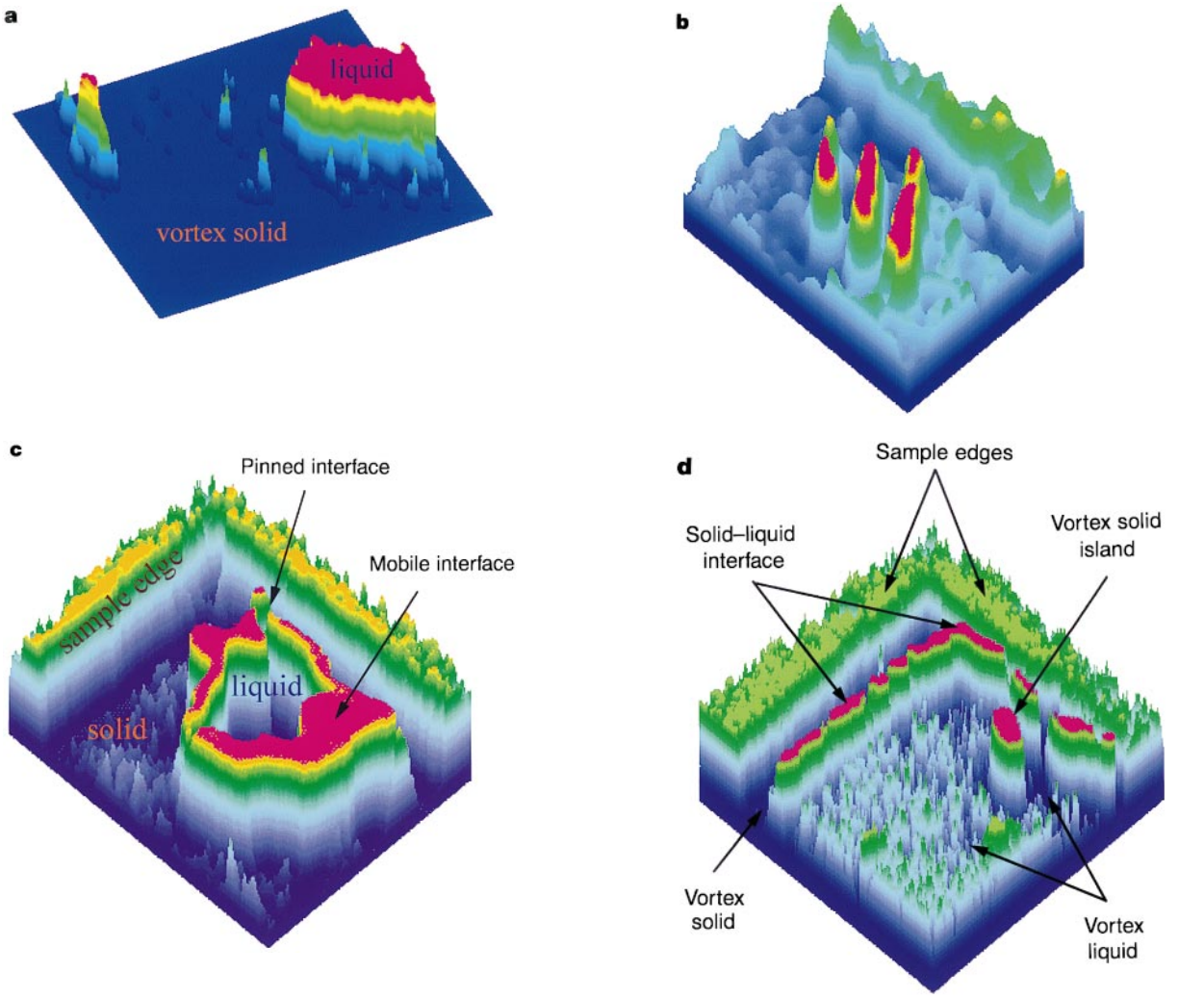

Figure 3 Four examples of melting features in various BSCCO crystals shown in a three-dimensional representation. The field scale from blue to magenta is about 0.3 G. Only selected parts of the samples are shown for clarity. **a**, Two liquid droplets (magenta) surrounded by vortex solid (blue). The smaller droplet on the left is only about seven vortices wide, demonstrating that disorder-assisted melting occurs on the scale of the inter-vortex distance. Image area $0.07 \times 0.14\,mm^2$, $H_a = 25.75$ Oe, $\delta H_a = 0.5$ Oe, and $T = 84$ K. **b**, Vortex liquid nucleation (magenta) occurring simultaneously in three adjacent finger-like regions. The image size is $0.24 \times 0.31\,mm^2$, $H_a = 38.5$ Oe, $\delta H_a = 1$ Oe, and $T = 80$ K. The top right side of the image shows one of the sample edges (green). **c**, An irregular vortex liquid region surrounded by vortex solid. The solid–liquid interface (magenta) is highly corrugated. In some regions the interface appears to be very wide due to its high mobility during the field modulation by δH_a. At other points the interface appears to be discontinuous due to interface pinning, which results in a lack of differential signal during field modulation. Outer edges of the sample are seen along the top sides of the image. $H_a = 83$ Oe, $\delta H_a = 0.5$ Oe, and $T = 70$ K. Image area is $0.26 \times 0.34\,mm^2$. **d**, A small vortex-solid island surrounded by vortex liquid. The liquid phase is in turn surrounded by vortex solid along the sample edges. The solid–liquid interface near the edges (magenta rim) appears highly non-uniform and discontinuous due to the alternating regions of mobile and pinned interface. The melting and freezing process of this solid island is characterized by a high degree of hysteresis, as shown in Fig. 4. Image area $0.68 \times 0.68\,mm^2$, $H_a = 69.5$ Oe, $\delta H_a = 0.5$ Oe, and $T = 75$ K.

width of the ring is a direct measure of the distance the interface expands due to δH_a. In some parts the ring is very broad, showing the locations where $H_m(x,y)$ has smooth, gradual behaviour (see Fig. 2a), resulting in a very mobile interface. In contrast, in other places where the ring appears to have discontinuities, the solid–liquid interface is effectively pinned due to steep $H_m(x,y)$. As the liquid domains expand with H_a, the peaks in $H_m(x,y)$ melt last, forming solid islands within the liquid (see Fig. 2a). Figure 3d depicts such a small solid island completely surrounded by vortex liquid, which in turn is surrounded by vortex solid along the edges of the crystal. In this configuration non-equilibrium phenomena are found to be present, as described below.

Our experimental results allow evaluation of the surface tension σ of the solid–liquid interface. Theoretically, the surface tension can be estimated as follows. At the first-order transition the discontinuous change in the internal energy is compensated by a change in the entropy, such that the free energy remains continuous. The jump in the energy density is roughly equal to $H_m\Delta B/4\pi$. If the solid–liquid interface has a width of the order of the inter-vortex spacing a_0, then within this width the system is neither liquid nor solid. Thus the energy cost per unit area of this interface can be estimated as $\sigma = \eta a_0 H_m \Delta B/4\pi$, where η is an unknown numerical factor presumed to be of order unity. When H exceeds a local minimum by $h = H - H_m$, a liquid droplet should be formed in a solid, provided the energy gain in melting is larger or equal to the energy cost of forming an interface. Assuming that the droplet is of radius r and that it extends throughout the thickness d of the sample, the energy gain is given approximately by $(\partial F_s/\partial H - \partial F_l/\partial H)h\pi r^2 d = \Delta B h r^2 d/4$. Here $\partial F_s/\partial H$ and $\partial F_l/\partial H$ are the derivatives of the free energies of the solid and liquid phases respectively, and we have used the fact that $\partial F_s/\partial H - \partial F_l/\partial H = \Delta B/4\pi$ at the melting transition. By comparing this gain with the interface energy $2\pi\sigma rd$, we obtain the minimum nucleation radius $r_{min} \approx 2\eta a_0 H_m/h$. The presented images show the existence of very small liquid droplets with $r_{min} \approx 3a_0$. By analysing the expansion of the droplets due to δH_a and upon varying H_a, we estimate the superheating h to be less than 0.5 Oe for a typical H_m of 50 Oe, which results in $\eta \leq 10^{-2}$. Thus, assuming that $H_m(x,y)$ exhibits smooth local behaviour, our measurements indicate that σ is two orders of magnitude lower than rough theoretical estimates. Such a low surface tension implies that the vortex melting process is completely governed by disorder and that the stabilizing influence of the interface[1] can be neglected. The origin of this phenomenon requires further investigation.

Hysteretic supercooling and superheating is an inherent property of a first-order transition[14], but the precise mechanism on a microscopic level is not clear. We are able to spatially resolve this unique feature, as shown in Fig. 4. We find that the hysteresis occurs only at the local maxima of $H_m(x,y)$, indicating that disorder is an important factor also in the non-equilibrium properties. In the top left image, at 68.50 Oe, a few vortex-solid islands are visible within the liquid in the upper part. As the field is increased, these solid islands split into smaller ones, and gradually shrink and disappear. At 69.50 Oe only one small island is left, visible as a bright spot, which fully melts at 69.75 Oe. A better view of the top-left corner of the sample including this island is shown in Fig. 3d. Upon decreasing H_a, the bright interface along the sample edges that separates the large central liquid region and the outer solid strips behaves

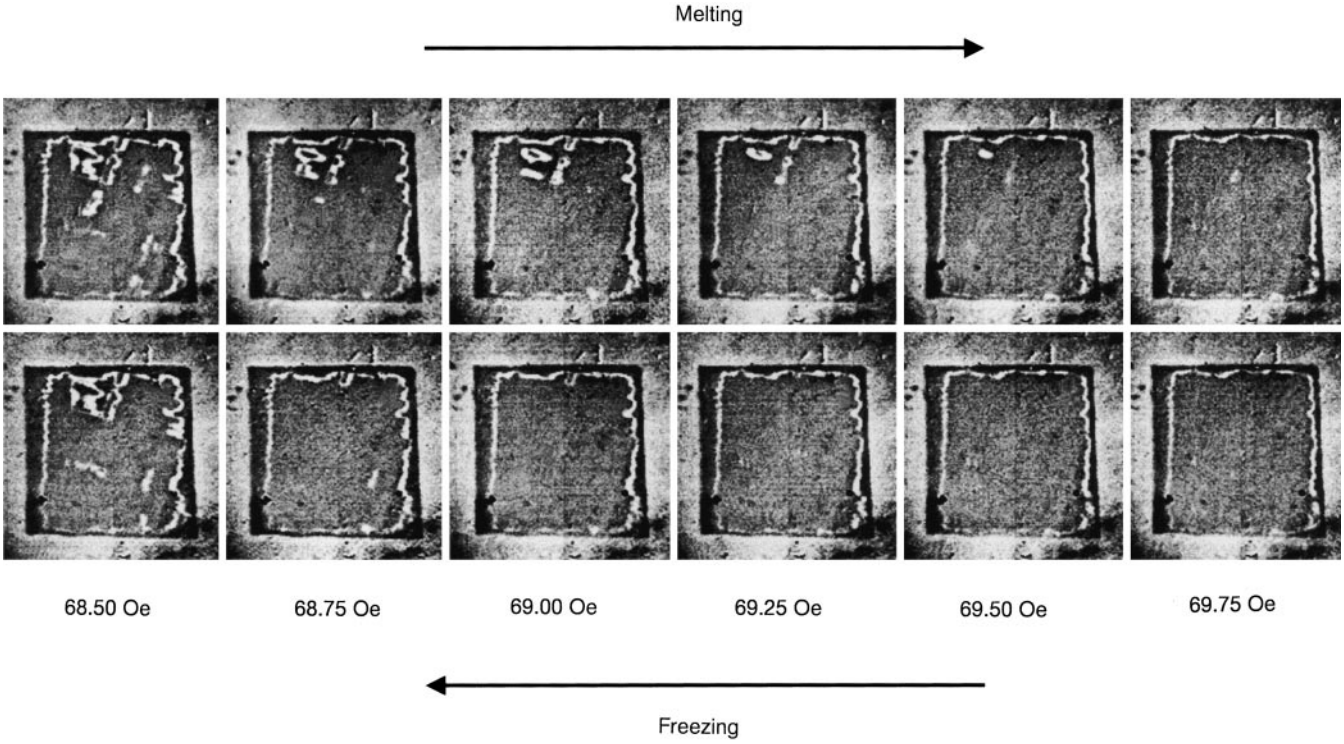

Figure 4 Direct visualization of the local supercooling and hysteresis process. The top row of images shows the melting sequence upon increasing the field, while the bottom shows the freezing process at the same values of decreasing field. The central region of the sample is in the liquid phase surrounded by vortex solid along the edges because of the dome-shaped field profile. The bright solid–liquid interface near the edges is highly corrugated due to the disorder-induced variations in the local $H_m(x,y)$, but it is completely reversible upon melting and freezing. In contrast, the behaviour of the solid islands, visible in the upper left part of the sample within the large liquid region, is highly hysteretic. In the melting sequence the islands shrink gradually until the last of the islands fully melts at 69.75 Oe. In the freezing sequence, however, the islands are absent and suddenly reappear only at 68.50 Oe, while the elongated central island nucleates at still lower field (not shown). In the four freezing images, 68.75 Oe through 69.50 Oe, in the areas where the islands are absent relative to the corresponding melting images, the liquid phase is in a supercooled state. These metastable supercooled liquid regions coexist with the surrounding equilibrium liquid. Such local supercooling is found only at local maxima of $H_m(x,y)$. No corresponding superheating of the solid is found at the minima of $H_m(x,y)$, and no hysteresis is observed in the regions where $H_m(x,y)$ varies monotonically. Sample size is $1.1 \times 1.2 \times 0.025\ mm^3$, $T = 75$ K and $\delta H_a = 0.5$ Oe. Small dark and bright spots that do not vary with field are defects in the MO indicator.

completely reversibly (compare the melting and freezing images at the same field). The inner solid islands, in contrast, are absent upon freezing, and then suddenly reappear at a lower field of 68.50 Oe. Once formed, the islands extend to their full size at the corresponding field, and proceed to behave reversibly as long as they are not fully melted again.

Reversible behaviour most probably reflects an equilibrium state of the system. The above results therefore imply that there is no supercooling or superheating when the solid–liquid interface is located in a region where the $H_m(x,y)$ landscape varies monotonically. The hysteretic behaviour occurs only when a new interface has to be formed, but only if this new interface surrounds a solid rather than a liquid. Hence, upon reducing H to below a local maximum of $H_m(x,y)$, the solid island is not readily formed (see lower panel of Fig. 2a). In this regime a unique situation occurs: metastable supercooled liquid domains, which are present instead of the 'missing' solid islands, coexist with the surrounding equilibrium liquid. Only when the supercooling becomes sufficiently large does sudden nucleation occur, upon which the solid abruptly occupies the entire volume of the supercooled domains. This non-equilibrium process is observed only at local maxima of $H_m(x,y)$. We would expect a symmetric non-equilibrium mechanism to be present at minima of $H_m(x,y)$, where superheated solid would transform hysteretically into a liquid droplet, but such hysteresis is not found. The asymmetry between the supercooling and superheating on a macroscopic scale is usually ascribed to the surface wetting process, which prevents solid superheating[14]. In our case mesoscopic vortex droplets are formed within a solid and therefore such an asymmetry should not be expected. Nevertheless, the tips of the vortices near the top and bottom surfaces of the crystal experience a reduced elastic confinement potential due to the absence of the lattice outside the sample. As a result, the vortex tips may undergo a pre-melting transition similar to the surface wetting in atomic solids, which may prevent the superheating of the vortex solid. In contrast to atoms, however, each vortex tip is attached to a solid vortex in the bulk, and therefore is restricted in space and may not exhibit liquid properties. □

Received 10 April; accepted 27 May 2000.

1. Imry, Y. & Wortis, M. Influence of quenched impurities on first-order phase transitions. *Phys. Rev. B* **19,** 3580–3585 (1980).
2. Blatter, G. *et al.* Vortices in high-temperature superconductors. *Rev. Mod. Phys.* **66,** 1125–1388 (1994).
3. Nelson, D. R. Vortex entanglement in high-T_c superconductors. *Phys. Rev. Lett.* **60,** 1973–1976 (1988).
4. Safar, H. *et al.* Experimental evidence for a first-order vortex-lattice-melting transition in untwinned single crystal $YBa_2Cu_3O_7$. *Phys. Rev. Lett.* **69,** 824–827 (1992).
5. Kwok, W. K. *et al.* Vortex lattice melting in untwinned and twinned single-crystals of $YBa_2Cu_3O_{7-\delta}$. *Phys. Rev. Lett.* **69,** 3370–3373 (1992).
6. Zeldov, E. *et al.* Thermodynamic observation of first-order vortex-lattice melting transition. *Nature* **375,** 373–376 (1995).
7. Zeldov, E. *et al.* Geometrical barriers in high-temperature superconductors. *Phys. Rev. Lett.* **73,** 1428–1431 (1994).
8. Indenbom, M. V. *et al.* Direct study of magnetic flux penetration and trapping in HTSC. *Physica C* **166,** 486–496 (1990).
9. Duran, C. A. *et al.* Real-time imaging of the magnetic flux distribution in superconducting $YBa_2Cu_3O_{7-\delta}$. *Nature* **357,** 474–477 (1992).
10. Welp, U. *et al.* Imaging of transport currents in superconducting $(Bi, Pb)_2SrCa_2Cu_3O_x$ composites. *Nature* **376,** 44–46 (1995).
11. Morozov, N. *et al.* Paramagnetic ac susceptibility at first-order vortex-lattice phase transition. *Phys. Rev. B* **54,** R3784–R3787 (1996).
12. Khaykovich, B. *et al.* Vortex-matter phase transitions in $Bi_2Sr_2CaCu_2O_8$: Effects of weak disorder. *Phys. Rev. B* **56,** R517–R520 (1997).
13. Oral, A. *et al.* Disorder-driven intermediate state in the lattice melting transition of $Bi_2Sr_2CaCu_2O_{8+\delta}$ single crystals. *Phys. Rev. B* **56,** R14295–14298 (1997).
14. Landau, L. D. & Lifshitz, E. M. *Statistical Physics* 3rd edn (Pergamon, Oxford, 1993).

Acknowledgements

We thank D. R. Nelson, Y. Imry, V. Vinokur, L. Balents, C. Varma, C. van der Beek and M. Indenbom for valuable discussions. This work was supported by the Israel Science Foundation and Center of Excellence Program, by the Ministry of Science, Israel, by the MINERVA Foundation, Munich, Germany, and by the Grant-in-Aid for Scientific Research from the Ministry of Education, Science, Sports and Culture, Japan.

Correspondence and requests for materials should be addressed to A. S. (email: hsasha@wisemail.weizmann.ac.il).

Optimal shapes of compact strings

Amos Maritan*, Cristian Micheletti*, Antonio Trovato* & Jayanth R. Banavar†

** International School for Advanced Studies (SISSA), Via Beirut 2–4, 34014 Trieste, Istituto Nazionale per la di Fisica della Materia (INFM) and the Abdus Salam International Center for Theoretical Physics, Trieste, Italy*
† Department of Physics and Center for Materials Physics, 104 Davey Laboratory, The Pennsylvania State University, University Park, Pennsylvania 16802, USA

Optimal geometrical arrangements, such as the stacking of atoms, are of relevance in diverse disciplines[1–5]. A classic problem is the determination of the optimal arrangement of spheres in three dimensions in order to achieve the highest packing fraction; only recently has it been proved[1,2] that the answer for infinite systems is a face-centred-cubic lattice. This simply stated problem has had a profound impact in many areas[3–5], ranging from the crystallization and melting of atomic systems, to optimal packing of objects and the sub-division of space. Here we study an analogous problem—that of determining the optimal shapes of closely packed compact strings. This problem is a mathematical idealization of situations commonly encountered in biology, chemistry and physics, involving the optimal structure of folded polymeric chains. We find that, in cases where boundary effects[6] are not dominant, helices with a particular pitch-radius ratio are selected. Interestingly, the same geometry is observed in helices in naturally occurring proteins.

The problem of placing spheres in three dimensions in order to attain the highest density was first posed by Kepler and has attracted much interest, culminating in its recent rigorous mathematical solution[1]. The close-packed hard-sphere problem may be restated in an alternative manner, more convenient for numerical implementation, as the determination of the arrangement of a set of points in a given volume that results in the minimum distance between any pair of points being as large as possible[6]. It is notable that the resulting 'bulk' optimal arrangement exhibits translational invariance in that, far from the boundaries, the local environment is the same for all points.

Here we introduce a new problem pertaining to the optimal shapes of compact strings. We consider a string (an open curve) in three dimensions. We use a geometric measure[7] of the curve, the 'rope length', defined as the arc length measured in units of the thickness, which has proved to be valuable in applications of knot theory[7–12]. The thickness Δ denotes the maximum radius of a uniform tube with the string passing through its axis, beyond which the tube either ceases to be smooth, owing to tight local bends, or it self-intersects. Our focus is on finding the optimal shape of a string of fixed arc length, subject to constraints of compactness, which would maximize its thickness, or equivalently minimize its rope length.

Following the approach of Gonzalez and Maddocks[10], who studied knotted strings, we define a global radius of curvature as follows. The global radius of curvature of the string at a given point is computed as the minimum radius of the circles going through that point and all other pairs of points of the string. It generalizes the concept of the local radius of curvature (the radius of the circle which locally best approximates the string) by taking into account both local (bending of the string) and non-local (proximity of another part of the string) effects. For discretized strings the local radius of curvature at a point is simply the radius of the circle going through the point and its two adjoining points. The minimum of all the global radii then defines the thickness, that is, the minimum radius of the circles going through any triplet of discrete points. This coincides with the previous definition in the continuum limit,